Role of oxygen vacancies on the low-temperature dielectric relaxor behavior in epitaxial Ba$_{0.85}$Ca$_{0.15}$Ti$_{0.9}$Zr$_{0.1}$O$_3$ thin films

Subhashree Chatterjee [1,*] Abhisikta Barman [1,*] Shubhankar Barman [2] Tanmay Chabri [1] Sohini Kar-Narayan [3]
Anuja Datta [2,3,†] and Devajyoti Mukherjee [1,‡]

[1]*School of Physical Sciences, Indian Association for the Cultivation of Science,*
2A & 2B Raja S. C. Mullick Road, Kolkata 700032, India
[2]*School of Applied and Interdisciplinary Sciences, Indian Association for the Cultivation of Science,*
2A & 2B Raja S. C. Mullick Road, Kolkata 700032, India
[3]*Department of Materials Science & Metallurgy, University of Cambridge,*
27 Charles Babbage Road, Cambridge CB3 0FS, United Kingdom

Dielectric relaxation in ferroelectric perovskites can result from different inherent chemical and charge disorders within their crystal structures. Despite several theories on dielectric relaxations, the relationship between the concentration of oxygen vacancy (V_O) and dielectric relaxation has not been studied in perovskite oxide thin films. In this work, we report a systematic investigation on the influence of the V_O's on the dielectric relaxation of Ba$_{0.85}$Ca$_{0.15}$Ti$_{0.9}$Zr$_{0.1}$O$_3$ (BCZT) epitaxial thin films grown with La$_{0.7}$Sr$_{0.3}$MnO$_3$ (LSMO) top and bottom electrodes on single-crystal SrTiO$_3$ (*100*) substrates using pulsed laser deposition. The ambient oxygen pressures during film growth were systematically varied to control the concentration of V_O in the epitaxial BCZT thin films. Low ambient oxygen pressure was found to enhance the tetragonality of the BCZT films and a systematic decrease in the tetragonality was observed at high oxygen pressure conditions as evidenced from x-ray diffraction (XRD) studies. Temperature dependent XRD analyses indicated a low-temperature anomaly near ∼160 K in the BCZT/LSMO heterostructures. Low-temperature dielectric measurements revealed relaxor dielectric response with broad frequency dependence of the dielectric constant. It is proposed that the low-temperature dielectric relaxation is possibly caused by dipolar clusters that are formed by the aggregation of correlated V_O-induced dipolar defects within the films deposited under different ambient oxygen pressures. High-resolution transmission electron microscopy suggested the presence of the nanometer-sized V_O clusters as represented by the structural defects of average diameters of ∼5 nm in the BCZT films grown at variable ambient oxygen pressure. Activation energies of the aforesaid dipolar clusters, obtained from the Vogel-Fulcher fitting of the dielectric dispersion, showed a gradual increase in magnitude, as well as decreasing freezing temperatures, with decreasing concentrations of V_O in the BCZT films. From the theoretical analysis of the experimental data, it is postulated that the presence of the V_O-induced dipolar defects affects the low-temperature dielectric relaxation in the BCZT thin films. This work significantly extends the understanding of V_O-mediated dielectric relaxor behavior in complex perovskite oxide films.

I. INTRODUCTION

Low-dimensional relaxor ferroelectric (FE) perovskites, such as thin films and heterostructures, exhibiting large dielectric and piezoelectric coefficients over broad temperature ranges, have attracted considerable attention for high-end industrial applications in sensors, transducers, actuators, microelectromechanical systems, electrocaloric coolers, energy harvesters, and energy storage devices [1–6]. With the environmental concerns on the toxicity of lead, in the last decade, several lead-free relaxor FE perovskites with high piezoelectric, dielectric, and polarization properties that are comparable to the industry-standard lead-based FE materials have emerged as promising candidates for replacing the lead-based materials in applications [7–10]. In recent years, large energy storage density, high energy harvesting efficiency, and huge pyroelectric/electrocaloric cooling effects have been reported in several lead-free relaxor FE thin films, which have raised their stakes as potential candidates for eco-friendly technological applications [11–15].

For practical applications of relaxor FE perovskites, it is crucial to understand the underlying mechanisms of their anomalous dielectric and polarization properties which have still remained elusive even after decades of their discovery in the classic lead-based relaxor PbMg$_{1/3}$Nb$_{2/3}$O$_3$ (PMN) [16]. One of the main difficulties in describing the relaxor behavior is due to the fact that relaxor materials typically have chemically disordered components well within the structurally ordered crystal lattices; causing them to behave as

---

*These authors contributed equally to this paper.
†Corresponding author: psuad4@iacs.res.in
‡Corresponding author: sspdm@iacs.res.in

dipolar glasses within certain temperature ranges [16,17]. ABO_3-type lead-based relaxors, for example, PMN, are characterized by nanoscale inhomogeneities occurring from the coexistence of the two types of B-site atoms, such as Mg^{2+} and Nb^{5+} in the structure. These heterovalent cations are inhomogeneously distributed to form chemically disordered regions, which are surrounded by ordered regions [16,17]. These "slushlike" charge disordered regions act as sources for random electric fields, which are believed to be responsible for the formation of polar nanoregions (PNRs) in these materials [16–18]. Direct observation of the formation of PNRs in the classic relaxors like PMN revealed that PNRs can coexist both within the normal FE domains (below the Curie temperature, T_C) and also within the paraelectric states (above T_C) in relaxor FE perovskites [19–21]. Although the exact origin of the ultrahigh piezoelectricity and dielectric permittivity observed in relaxor FE crystals have remained an open question, it is believed that these unusually high properties arise from the dynamics of the spatially hierarchical PNRs formed within these relaxor materials [20,21].

In terms of lead-free materials, the FE perovskite, $Ba_{0.85}Ca_{0.15}Zr_{0.1}Ti_{0.9}O_3$ (BCZT) is particularly promising due to its significant dielectric constant ($\sim$8000–15 000) and FE properties (remanent polarization $P_r \approx$ 10–15 $\mu C\,cm^{-2}$, and coercive field $E_C \approx$ 1.5–3 kV cm^{-1}) near room temperature in combination with a large piezoelectric coefficient ($\approx$620 pC N^{-1}), that is comparable to the lead-based $PbZr_xTi_{1-x}O_3$ (PZT) [22–26]. The phase diagram of the BCZT bulk system exhibits a "tilted" morphotropic phase boundary (MPB) separating the rhombohedral (R) and the tetragonal (T) phases [22,27,28]. The specific composition of $Ba_{0.85}Ca_{0.15}Zr_{0.1}Ti_{0.9}O_3$ (BCZT) studied here is near the MPB, which makes this composition easily poled and switchable due to external stress or electric fields [29–33]. Like the lead-based relaxors, the relaxor behavior in BCZT ceramics is also believed to arise from the local random fields associated with the cation disorder resulting from the partial cosubstitution of Ba^{2+} (A site) by Ca^{2+} and Ti^{4+} (B site) by Zr^{4+} in the parent compound $BaTiO_3$ (i.e., ABO_3) [32–39]. However, the origin of the random fields in the homovalent substituted BCZT is different from that of the heterovalent substitution in lead-based relaxors such as PMN due to the absence of any charge disorder in BCZT [32–39]. It is believed that the disordered distribution of Ti^{4+} and Zr^{4+} ions on the B sites of BCZT, which exhibit only a small difference in their ionic radii, gives rise to the emergence of local random fields which lead to the relaxor behavior observed in BCZT ceramics [40–42]. On the other hand, the relaxor behavior of the parent compound $BaTiO_3$ has been attributed to its order-disorder phase transition due to the presence of electric dipoles arising from the off-centering of Ti in the [*111*] direction in a $BaTiO_3$ (*111*) single crystal [43]. Low-temperature dielectric dispersion of the $BaTiO_3$ (*111*) single crystal showed broad transition peaks near 100 K like the FE relaxors and obeyed the Vogel-Fulcher freezing behavior similar to that observed in dipolar glasses [44,45]. Further studies have confirmed the existence of nanoscale local dipolar structures in $BaTiO_3$ due to Ti off-centering in either [*111*] or [*100*] directions creating the order-disorder characters both in the orthorhombic and the tetragonal phases which showed to influence the low-

temperature dielectric relaxation [46]. These reports indicate that it is also possible to interpret the dielectric relaxations in $BaTiO_3$ based systems (viz., BCZT) as being attributed to local dipoles as opposed to the mechanism of dynamic PNRs typically associated with the classic FE relaxors.

In terms of thin films, enhanced dielectric relaxor properties have been reported in polycrystalline BCZT thin films prepared by various chemical and physical routes [47–49]. Strain enhanced FE properties have been reported in epitaxial BCZT (*001*) thin films grown on conductive Nb-doped (*001*)-$SrTiO_3$ single-crystal substrates (P_r = 21.3 $\mu C\,cm^{-2}$ at E_C = 60 kV cm^{-1}) [50] and in epitaxial $La_{0.67}Ca_{0.33}MnO_3$/BCZT heterostructures (P_r = 10.3 $\mu C\,cm^{-2}$ at E_C = 220 kV cm^{-1}) grown on MgO (*100*) substrates [51]. Recently, large electrocaloric effects have been reported in bilayer thin films of $(Bi_{0.5}Na_{0.5})TiO_3$−$BaTiO_3$ (BNBT)-BCZT and epitaxial BCZT (*001*) thin films [13,52]. All these reports have spurred the investigations on the underlying mechanisms of relaxor behavior in BCZT thin films for applications.

Recently, it has been theoretically predicted that relaxor behavior in FE perovskites can also be controlled by the presence of oxygen vacancy (V_O) concentrations, [53] apart from the inherent chemial disorder phenomena. The presence of V_O in FE perovskites greatly influences their physical properties since the perovskite structure is able to conserve its structural stability even for high concentrations of V_O [54]. Scott *et al.* reported that V'_Os in FE perovskites generally aggregate to form nanoscale dipolar clusters due of the existence of strong correlation among them since the V'_Os interact with the off-centered B-site ions creating dipolar defects in ABO_3 perovskites [53,55]. The activation energies of these dipolar clusters are inversely proportional to the concentration of V'_Os since the energy for the collective movement of one cluster is much lower than the summation energy for the movement of individual V'_Os [56]. With the increasing concentrations of V'_Os, the defect dipole concentrations also increase and consequently the correlation among the dipolar defects strengthen leading to formation of dipolar clusters with decreasing the activation energies [57–59]. At the low-temperature regime, the dipolar clusters are "frozen in", however, they can be thermally activated with increasing temperatures to induce dielectric relaxations, as reported in some perovskite ceramics [60,61]. Experimentally, the concentration of V_O in oxide thin films can be manipulated by varying the deposition conditions such as the ambient oxygen environment during the film growth in physical techniques such as pulsed laser deposition (PLD) [62]. Thus, a systematic investigation on thin films of the promising FE perovskite BCZT could open up new directions to understand the role of V_O and to govern their relaxor properties, which are both fundamentally interesting and technologically important. However, the relationship between V_O and dielectric relaxation has been rarely studied in perovskite thin films [57]. Li *et al.* reported that that the dipolar defects created by V_O interacting with the off-centered Ti ions resulted in the dielectric relaxation in perovskite $Eu_{0.5}Ba_{0.5}TiO_{3-\delta}$ epitaxial films [57]. To the best of our knowledge, a systematic investigation on the influence of V_O on the relaxor behavior of epitaxial BCZT thin films has not been reported to date. This type of study could potentially pave the way for further research into the fundamental understanding of the relaxor

behavior in BCZT thin films and their associated electrocaloric, high efficiency energy storage and conversion applications.

In this work, the role of V_O on the low-temperature dielectric relaxor properties of $Ba_{0.85}Ca_{0.15}Ti_{0.9}Zr_{0.1}O_3$ (BCZT) thin films are studied in detail. The focus on the low-temperature dielectric properties in BCZT thin films potentially carries significance for the scientific understanding of the relaxor behavior of the system. Epitaxial BCZT thin films were grown on top of bottom electrodes comprising the ferromagnetic half-metal, $La_{0.7}Sr_{0.3}MnO_3$ (LSMO) on single crystal $SrTiO_3$ (STO) (*100*) substrates by PLD technique [50] under varying ambient oxygen pressures (P_{O_2}) (keeping other deposition parameters constant), in order to control the concentration of Vo incorporated during film growth [63–65]. The lattice-matched LSMO electrodes were strategically used to minimize the space-charge effects at the dielectric-electrode interface in the sandwich BCZT/LSMO capacitor structure. Note that space charge effects of V_O in BCZT films have been exclusively investigated previously [65]. Detailed x-ray diffraction (XRD) studies revealed a systematic decrease in the tetragonality of BCZT thin films with an increase in P_{O_2} during film growth. Low-temperature x-ray analyses revealed an anomaly around 160 K in the BCZT thin films. Low-temperature dielectric properties revealed a broad dielectric dispersion indicating the relaxor behavior in the BCZT thin films. The dielectric relaxations were attributed to the formation of dipolar clusters created by the V_O induced defect dipoles within the BCZT films grown under different P_{O_2} conditions. The freezing temperatures and activation energies of the dipolar clusters, obtained from the Vogel-Fulcher fitting of the dielectric dispersion, showed a systematic change with varying concentrations of the V_O's in the BCZT films. A phenomenological model is proposed to explain the observed close correlation between the activation energy and V_O in the BCZT thin films. The work provides fundamental insight into V_O mediated dielectric relaxor behavior in BCZT thin films and adds to the knowledge of the structure-property relationship in lead-free FE perovskite heterostructures with enhanced properties.

II. EXPERIMENT

BCZT thin film heterostructures using LSMO top and bottom electrodes were fabricated on single-crystal STO (*100*) substrates using a commercial PLD (Neocera Pioneer 120 Advanced) system. Briefly, high-purity ceramic targets of $La_{0.7}Sr_{0.3}MnO_3$ and $Ba_{0.85}Ca_{0.15}Ti_{0.9}Zr_{0.1}O_3$ were prepared using commercially bought powders from Alfa Aesar with high purity (99.99%) via cold pressing followed by sintering at 1200 °C. The prepared targets were characterized for phase purity and composition. The LSMO and BCZT targets were then sequentially ablated using a KrF excimer laser (Lambda Physik, $\lambda = 248$ nm, frequency = 10 Hz, fluence = 3 J cm^{-2}) inside a deposition chamber equipped with a multitarget carousel that allowed for the *in situ* deposition of multilayers with clean interfaces. A distance of 5 cm was maintained between the substrate and the targets during the depositions. Prior to growing the LSMO layer, the STO substrate was annealed inside the PLD chamber at 800 °C under

an ambient P_{O_2} of 500 mTorr for 2 h. In the optimized synthesis process, an initial layer of LSMO was deposited onto an STO substrate at 800 °C under a P_{O_2} of 10 mTorr, followed by the BCZT layer at 750 °C with different P_{O_2} of 0.1, 0.5, and 1 Torr, respectively. A shadow mask was used during the BCZT layer deposition to preserve an open access to the LSMO bottom electrode. After the BCZT layer deposition, top LSMO electrodes of 200 μm in diameter and 100 nm thickness were deposited using a shadow mask at 750 °C under a P_{O_2} of 10 mTorr. After deposition, the samples were gradually (~4 h) cooled down to room temperature. The thicknesses of the LSMO and BCZT layers were kept constant at ~100 and ~120 nm, respectively. The crystallinity and crystallographic orientations in the heterostructures were characterized by XRD with a Rigaku Smart Lab 9 kW XG diffractometer equipped with a five-axis goniometer and temperature variable thin film sample stage using collimated parallel beam Cu-$K\alpha$ radiation ($\lambda = 1.5406$ Å). Thermal conductive Apeizon N grease was used to fix the samples on the thin film temperature stage of the XRD and care was taken to avoid sample misalignment. Raman spectra were measured at room temperature using a laser Raman spectrophotometer (JY Horiba-T6400 equipped with a Synopse charge-coupled device camera) using a Nd:YAG laser (532 nm) over the range $150-900$ cm^{-1}. The Raman spectra reported here have been de-convoluted into individual Lorentzian peaks for accurate peak positioning. X-ray photoelectron spectra (XPS) were measured using a commercial Omicron (model 1712-62-11) spectrometer. The data were collected at room temperature using a nonmonochromatic Al $K\alpha$ (1486.7 eV) x-ray source operating at 150 W (15 kV and 10 mA). The interfacial microstructure in the BCZT/LSMO heterostructure was analyzed using high-resolution transmission electron microscopy (HRTEM; FEI Tecnai F 20 S-Twin TEM). A sample for cross-sectional TEM analysis was prepared by surface milling a 5 μm $\times$ 10 μm rectangular strip of 100 nm thickness using a focused ion beam (FIB; JOEL 4500 FIB/SEM) and Pt-welding it to a Cu TEM grid. Temperature dependent dielectric properties were measured at different frequencies using a Keysight E4980A Precision LCR meter equipped with a commercial low-temperature cryostat (CFMS, Cryogenic Ltd.) after proper calibration.

III. RESULTS AND DISCUSSION

To maintain simplicity in discussion, henceforth in the text, the BCZT thin films grown under different P_{O_2} of 0.1, 0.5, and 1 Torr, keeping other PLD parameters constant, will be denoted as BCZT(0.1T), BCZT(0.5T), and BCZT(1T), respectively.

A. Crystallinity and surface morphology

The unit cell crystal structure and lattice parameters for the bulk BCZT target were tetragonal with $c = 4.012$ Å and $a = b = 4.005$ Å, as obtained from the Rietveld refinement of the room-temperature XRD θ-2θ pattern as shown in Fig. 1(a) [66]. The details of the structural refinement and the compositional analyses using energy dispersive spectroscopy of the BCZT target are shown in the Supplemental Material [67]
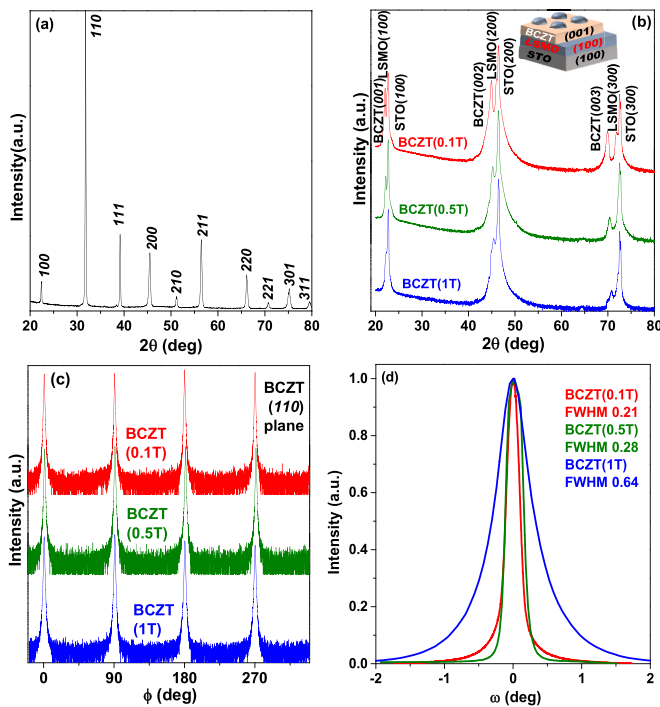
FIG. 1. Room-temperature XRD θ-2θ patterns of (a) BCZT bulk target and (b) BCZT(0.1T), BCZT(0.5T), and BCZT(1T) thin films, respectively. Inset to (b) shows the schematic of the BCZT/LSMO/STO heterostructure. (c) XRD ϕ scans performed about BCZT (*110*) plane and (d) XRD ω scans performed about the BCZT (*001*) plane for BCZT(0.1T), BCZT(0.5T), and BCZT(1T) thin films, respectively.

FIG. 2. (a) XRD symmetric θ-2θ scans about the BCZT (*002*) plane, (b) XRD asymmetric 2θ-ω scans about the BCZT (*111*) plane for BCZT(0.1T), BCZT(0.5T), and BCZT(1T) thin films, respectively. (c) Out-of-plane (c) and in-plane (a) lattice parameters and (d) tetragonality in BCZT(0.1T), BCZT(0.5T), and BCZT(1T) thin films plotted with respect to the ambient P_{O_2} condition during growth. The dotted line shows the corresponding value of bulk lattice parameter of BCZT target.

(Figs. S1 and S2). The crystalline structure of the BCZT target was also confirmed using Raman spectra and matched with the XRD analyses as shown in the Supplemental Material [67] (Fig. S3) [68,69]. From the above XRD analyses, it is observed that the bulk BCZT (tetragonal, $c = 4.012$ Å and $a = b = 4.005$ Å) has a small lattice mismatch ($\sim 3.5\%$) with the underlying LSMO layer (pseudocubic, $a = 3.87$ Å) and the STO (*100*) substrate (cubic, $a = 3.905$ Å), which allowed for the epitaxial growth of the BCZT/LSMO/STO heterostructures [shown schematically in the inset to Fig. 1(b)]. The single crystalline nature of the BCZT and LSMO phases in BCZT/LSMO heterostructures are evident from the XRD θ-2θ patterns shown in Fig. 1(b). In all cases, only strong (*00l*) ($l = 1$, 2, and 3) diffraction peaks of the tetragonal BCZT phase [as indexed with the refined bulk BCZT structure shown in Fig. 1(a)] were observed along with the (*l00*) ($l = 1$, 2, and 3) peaks of the pseudocubic perovskite LSMO phase (JCPDS 01-089-4461) and the single-crystal STO (*100*) substrate, confirming the unidirectional cube-on-cube epitaxial growth, with no traces of impurity peaks within the resolution limits of the XRD. A decrease in the XRD peak intensities in Fig. 1(b) from BCZT(0.1T) to BCZT(1T) could be due to the loss of crystallinity with depositions under higher P_{O_2} conditions. Azimuthal (ϕ) scans were performed about the BCZT (*110*) crystallographic planes to confirm the epitaxial relationships of the BCZT thin films. Figure 1(c) shows a representative ϕ scan pattern; where the occurrence of peaks at regular intervals of 90° is a consequence of the fourfold cubic
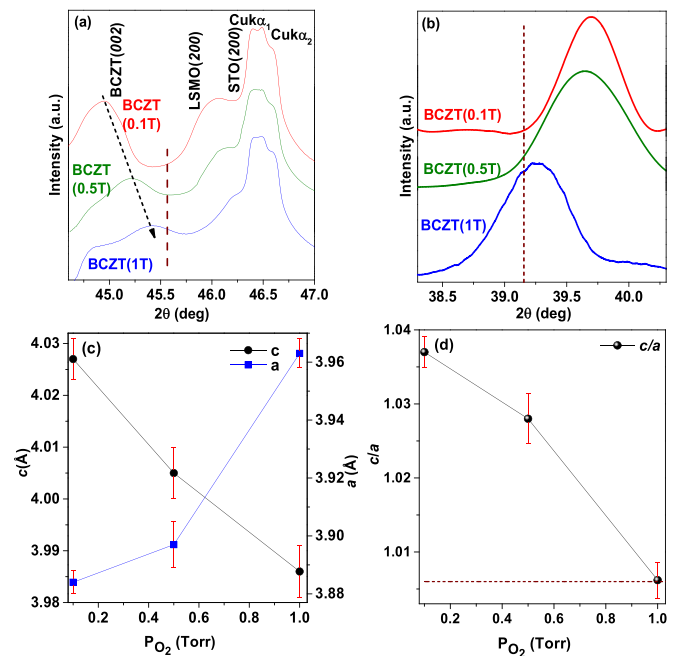
symmetry of the BCZT layer in the films. Rocking curves (ω scans) performed about the BCZT (*001*) crystallographic planes for the films shown in Fig. 1(d) yielded peaks with a narrow full width at half maximum (FWHM) (0.2–0.6°) values, confirming the excellent in-plane orientation of the BCZT (*001*) layers. The rocking curves were fitted using the pseudo-Voigt function which is a linear combination of Lorentzian and a Gaussian function [70]. A slight relaxation of the in-plane texturing was observed with the increasing FWHM values in Fig. 1(d) from BCZT(0.1T) to BCZT(1T) with depositions under higher P_{O_2} conditions.

Figure 2(a) shows the XRD symmetric θ-2θ scans near the BCZT (*002*) planes with close proximity of the LSMO (*200*) and STO Cu-$K_{\alpha 1}$ and Cu-$K_{\alpha 2}$ (*200*) peaks for the BCZT(0.1T), BCZT(0.5T), and BCZT(1T) thin films, respectively. The vertical dotted line represents the position of the (*002*) peak in bulk BCZT target [see Fig. 1(a)]. A distinct shift of the XRD peaks to higher 2θ values [dotted arrows in Fig. 2(a)] was observed from BCZT(0.1T) to BCZT(1T) films as the P_{O_2} increases from 0.1 to 1 Torr with respect to the unchanging LSMO and STO (*200*) substrate peak positions [71]. From Fig. 2(a) it can be inferred that a decrease in the out-of-plane lattice parameter (c) occurs in the tetragonal BCZT films as the P_{O_2} concentration increases from 0.1 to 1 Torr. On the other hand, asymmetric 2θ-ω scans about the BCZT (*111*) planes in the BCZT(0.1T), BCZT(0.5T), and BCZT(1T) thin films, as shown in Fig. 2(b), exhibited a large shift in XRD peaks to lower 2θ values as the P_{O_2} increases from 0.1 to

TABLE I. Structural and low temperature dielectric properties of $Ba_{0.85}Ca_{0.15}Ti_{0.9}Zr_{0.1}O_3$ (BCZT) (*001*) thin films grown with varying ambient oxygen pressures (P_{O_2}) as detailed in the text: lattice parameters (c and a), tetragonality (c/a), (Ti + Zr)/(Ba + Ca) site occupancy ratio, relative peak area (RPA) ratio of Ti^{3+} to Ti^{4+} and O1s b to O1s a, % of V_O, maximum dielectric constant ($\varepsilon'_{r_{max}}$), transition temperature (T_m), degree of diffusiveness (D') at 1 kHz, and activation energy (E_a) and freezing temperature (T_{VF}) of dipolar-cluster formed by V_O-related defect dipoles from Vogel-Fulcher fitting.

Sample	P_{O_2}	c	a	c/a	(Ti+Zr)/	RPA ratio		V_O	$\varepsilon'_{r_{max}}$	T_m	D'	E_a	T_{VF}
	(Torr)	(Å)	(Å)		(Ba+Ca)	Ti^{3+}/Ti^{4+}	O1s b/O1s a	(%)		(K)		(eV)	(K)
BCZT(0.1T)	0.1	4.03	3.884	1.037	0.98	0.85	0.44	9.0 ± 0.2	844	149	48	0.04	116
BCZT(0.5T)	0.5	4.01	3.897	1.028	1.12	0.61	0.27	6.4 ± 0.5	806	153	52	0.07	96
BCZT(1T)	1	3.99	3.963	1.006	1.22	0.44	0.18	2.3 ± 0.6	650	154	57	0.09	80

1 Torr, as compared to the bulk BCZT (*111*) peak shown by the vertical dotted line. The BCZT planes for the asymmetric scans were carefully chosen such that there were no contributions to the XRD peaks from the underlying LSMO or STO layers. The lattice parameters (a and c) of the tetragonal BCZT unit cell were calculated for the BCZT (*001*) films from the detailed XRD symmetric and asymmetric scans, respectively. Table I summarizes the lattice parameters (a and c) and tetragonality (c/a) for the BCZT (*001*) films. Due to the epitaxial strain of the underlying LSMO layer, the BCZT layer might have experienced an in-plane compressive and an out-of-plane tensile strain in all the films, respectively. From Table I, it is observed that the BCZT(0.1T) film exhibited enhanced tetragonality of $c/a = 1.037$ as compared to that of the unstrained BCZT bulk of $c/a = 1.002$. However, with increase in P_{O_2} in the BCZT(0.5T) and BCZT(1T) thin films, the tetragonality was systematically decreased as compared to the BCZT(0.1T) film which could be possibly due to the lower concentration of V_O in the BCZT films grown at higher P_{O_2} conditions. In Fig. 2(c), we plot the lattice parameters (c, a), and in Fig. 2(d), we plot tetragonality (c/a) values for BCZT unit cells in the BCZT (*001*) films as a function of P_{O_2}. From Fig. 2(c) it is clearly observed that the c values monotonically decrease, while the a values correspondingly increase as P_{O_2} increases from 0.1 to 1 Torr (see Table I). This resulted in an almost 3% enhancement in the tetragonality (c/a) of the BCZT(0.1T) film ($c/a = 1.037$) with respect to the BCZT(1T) film ($c/a = 1.006$) as can be seen in Fig. 2(d). From the above XRD analyses, it is confirmed that depositions with higher P_{O_2} affected (i.e., decreased) the tetragonality of the BCZT unit cells in the BCZT (*001*) films, possibly as a result of decreased concentration of V_O with depositions under higher P_{O_2} conditions. Nonetheless, since the specific composition of BCZT in this case is near its MPB, even such small changes (2–3%) in the tetragonality of the BCZT unit cell due to variation in V_O could have a profound effect on its dielectric properties. High degrees of tetragonal distortion (i.e., $c/a - 1$) in BCZT thin films and nanostructures led to enhanced Curie temperatures (T_C) as reported in epitaxial BCZT (*001*) thin films ($T_C = 430$ K with $c/a - 1 = 2.3\%$) [13] and oriented BCZT nanowires ($T_C = 573$ K with $c/a - 1 = 4\%$) [23] as compared to the unstrained BCZT bulk ceramics with

lower tetragonality ($T_C = 363$ K with $c/a - 1 = 0.2\%$) [24]. It is often argued that the epitaxial strain and crystallographic orientations govern the formation and ordering of V_O in perovskite thin films [72]. During the PLD process under low P_{O_2} conditions (i.e. $P_{O_2} = 0.1$ Torr), the laser ablated species of the BCZT target in the forward directed plasma-plume encounter less collisions with the ambient O_2 as compared to that in the higher P_{O_2} conditions. Thus, the ablated species have higher kinetic energies and adatom mobility on reaching the substrate along the perpendicular direction of the substrate plane which creates higher concentrations of V_O (i.e., along the [*001*] direction), in the BCZT(0.1T) thin film as compared to BCZT(0.5T) and BCZT(1T) films. The concentration of V_O in the BCZT perovskite structure could create structural irregularities which impart higher tetragonality to the BCZT(0.1T) unit cell, similar to epitaxial $BaTiO_3$ films grown using PLD under different P_{O_2} conditions [63,73–75].

X-ray photoelectron spectroscopy (XPS) data were collected *ex situ* from the BCZT (*001*) thin films to determine the composition and the site occupancy of the ions in the BCZT unit cells. Figure 3(a) shows the core level XPS spectra of Ba 3d, Ti 2p, Ca 2p, and Zr 3d for the BCZT(0.1T), BCZT(0.5T), and BCZT(1T) thin films, respectively. From Fig. 3(a), a slight increase in the binding energies of Ba 3d (Ba 3$d_{5/2}$ from 780 to 782 eV and Ba 3$d_{3/2}$ from 795 to 797 eV), Ca 2p (Ca 2$p_{3/2}$ from 346 to 348 eV and Ca 2$p_{1/2}$ from 350 to 352 eV), Ti 2p (Ti 2$p_{3/2}$ from 457 to 458 eV and Ti 2$p_{1/2}$ from 464 to 466 eV), and Zr 3d (Zr 3$d_{5/2}$ from 184.1 to 185 eV and Zr 3$d_{5/2}$ from 181 to 183 eV) (shown by dotted arrows) can be observed for the BCZT(0.1T), BCZT(0.5T), and BCZT(1T) thin films, respectively. The systematic increase of the binding energies of each of the constituent elements in the BCZT (*001*) films indicates their higher oxidation states achieved with depositions under increasing P_{O_2} conditions. The composition of the BCZT thin films as calculated from the XPS analyses is $Ba_{0.85\pm0.02}Ca_{0.15\pm0.02}Ti_{0.90\pm0.01}Zr_{0.10\pm0.01}O_3$, which is close to the nominal composition of BCZT ($Ba_{0.85}Ca_{0.15}Ti_{0.90}Zr_{0.10}O_3$). Table I also shows the B to A site (for ABO_3 perovskite structure) [i.e., (Ti+Zr)/(Ba+Ca)] cationic occupancy ratios for the BCZT thin films as calculated from the XPS spectra in Fig. 3(a). From Table I it can be seen that the cationic stoichiometry is slightly affected by the
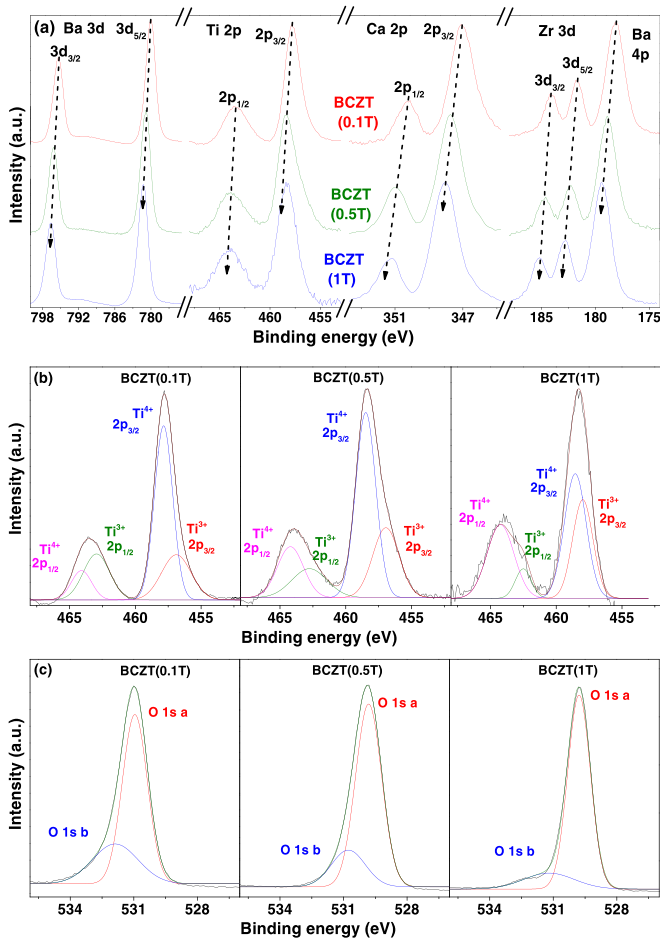
FIG. 3. (a) XPS spectra of (a) Ba $3d$, Ca $2p$, Ti $2p$, and Ba $4p$, Zr $3d$ states for BCZT(0.1T), BCZT(0.5T), and BCZT(1T) thin films, respectively. High resolution XPS spectra for (b) Ti $2p$ levels and (c) O $1s$ levels for BCZT(0.1T), BCZT(0.5T), and BCZT(1T) thin films, respectively.

P_{O_2} during the film growth since for the ideal stoichiometric growth B site/A site, i.e., the (Ti + Zr)/(Ba + Ca) ratio should be equal to 1. From the table, it can be seen that at low P_{O_2}, the A site cationic occupancy is higher than the B site, as in BCZT(0.1T), whereas the opposite nature is observed in BCZT(1T) grown at higher P_{O_2} [64]. The different cationic ratios observed in the thin films grown under varying P_{O_2} could affect their polarization and dielectric properties since these are primarily governed by the ionic displacements of the cations in the BCZT unit cell, as reported in other perovskites [74–76].

It is known that within the BCZT perovskite unit cell, near the neighborhood of a V_O, in order to compensate for the loss of oxygen negative charges (O^{2-}), an equivalent amount of Ti^{4+} ions typically get transformed to Ti^{3+} ions [53]. The electrons necessary for the transformation of Ti^{4+}/Zr^{4+} into Ti^{3+}/Zr^{3+} are created from ionization of neutral oxygen vacancy $V_O \rightarrow V_O^{\bullet} + e$, $V_O^{\bullet} \rightarrow V_O^{\bullet\bullet} + e$, $V_O^{\bullet}$ and $V_O^{\bullet\bullet}$ being positively charged V_O's [53]. Thus, the relative concentration of the Ti^{3+} ions with respect to the Ti^{4+} ions is expected to be higher for BCZT thin films grown under low P_{O_2} conditions [77–79]. In order to estimate the concentration

of V_O in the BCZT (*001*) films, the ratio of areas for Ti^{3+} and Ti^{4+} peaks from the high-resolution XPS spectra as shown in Fig. 3(b) was calculated as listed in Table I [77–79]. It is noted that the Ti $2p_{3/2}$ and Ti $2p_{1/2}$ doublets in Fig. 3(b) arising from the spin orbit splitting of the Ti $2p$ levels have binding energy differences $\sim$5.5–5.8 eV which is consistent with the reported values for BCZT ceramics [69,78]. From the listed values in Table I, it is clearly observed that the concentration of Ti^{3+} to Ti^{4+} gradually decreases with higher P_{O_2} conditions from BCZT(0.1T) to BCZT(1T). The higher ratio of Ti^{3+} to Ti^{4+} peak areas in the XPS spectra possibly indicates higher concentration of V_O for the BCZT(0.1T) thin film, which gradually decreases in the BCZT(0.5T) and BCZT(1T) films at higher P_{O_2} conditions, respectively. The percentages of V_O per unit cell in the BCZT(0.1T), BCZT(0.5T), and BCZT(1T) films were calculated from the relative peak area ratios of the Ti^{3+} and Ti^{4+} peaks as shown in the XPS spectra in Fig. 3(b) and listed in Table I. Here, we assume that the contribution of Ti^{3+} peaks in the XPS spectra in Fig. 3(b) mainly arises from the transformation of partial Ti^{4+} ions to Ti^{3+} ions in the perovskite BCZT unit cell in order to maintain charge neutrality due to the presence of V_O [80,81]. Similar XPS analyses of the BCZT (*001*) films reveal that the ratio of peak areas for the O $1s$ level as shown in Fig. 3(c) indicates higher values for BCZT(0.1T) films which gradually decrease in BCZT(0.5T) and BCZT(1T) films with increasing P_{O_2} conditions (as listed in Table I). It is noted that the O $1s$ level in the XPS spectra in Fig. 3(c) has been deconvoluted in two peaks, the major peak (O $1s$ a) with lower binding energy is associated with the lattice oxygen and the minor peak (O $1s$ b) with higher binding energy is associated with mainly due to V_O formation in perovskite oxides [82]. The XPS analyses thereby also confirms that there is a systematic decrease in the percentage of V_O per BCZT unit cell from as high as $\sim$9% in the BCZT(0.1T) film to $\sim$6% in the BCZT(0.5T) film to as low as $\sim$2% in the BCZT(1T) film (Table I).

HRTEM is regularly used to locate defects in many thin film and nanostructures [83–85]. A typical cross sectional representative HRTEM image of the BCZT(0.1T) film [Fig. 4(a)] shows sharp interface (dotted lines) with the LSMO bottom layer and respectively with the STO substrate. Similar cross-sectional HRTEM images were also obtained from the BCZT(0.5T) and BCZT(1T) films. The highly ordered crystallinity and lattice arrangements in BCZT(0.1T) film and BCZT(1T) film are clearly exhibited in the HRTEM images in Figs. 4(b) and 4(c) of the BCZT(0.1T) and BCZT(1T) films, respectively, taken under two beam conditions. The in-plane (*100*) lattice parameter in both BCZT (0.1T) and BCZT(1T) films are calculated to be $\sim$0.39 nm and $\sim$0.40 nm, which match well with that of calculated values from XRD (Table I). In Fig. 4(b), HRTEM of BCZT(0.1T) film additionally shows a high density of dark spots, which are correlated often with the V_O defects in many reports [86–90]. Together as clusters, the vacancy spots may create nanodomains, which are $\sim$5–7 nm in longest diameters here, as seen from Fig. 4(b). Upon closer inspection, the defects appear as isolated spots or oblong clusters largely in BCZT(0.1T) film, but sporadically as smaller single spots in the BCZT(1T) film, showing a clear decreasing trend due to higher P_{O_2} during deposition. The
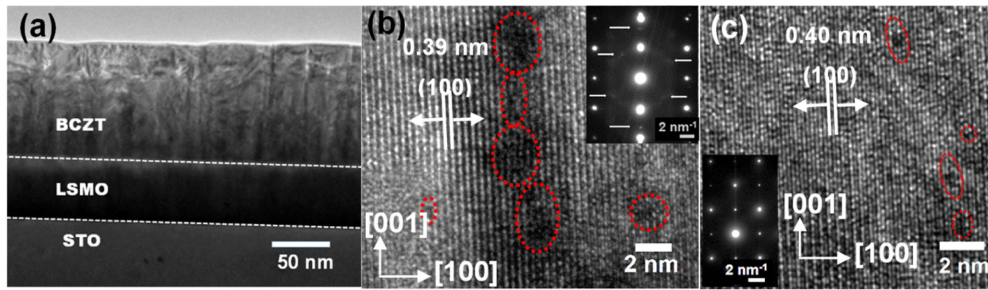
FIG. 4. (a) Cross sectional representative HRTEM image of BCZT(0.1T) thin film. HRTEM image of highly ordered crystallinity and lattice arrangements in (b) BCZT(0.1T) and (c) BCZT(1T) films taken under two beam conditions, respectively. Red dotted regions denote the nanodomains created by oxygen vacancy defects. Insets to (b) and (c) show the SAED patterns of the BCZT(0.1T) and BCZT(1T) films, respectively.

samples were scrutinized in several areas and a similar trend was uniformly observed throughout. Insets of Figs. 4(b) and 4(c) show SAED patterns of the corresponding films. The strong reflections in the SAED patterns are associated with the tetragonal structure of BCZT, whereas the weak reflections (indicated by arrows) at $\frac{1}{2}$ reflection sites might originate from the V'_Os as observed for the BCZT(0.1T) film. For the [100] direction, vertical domain structures and spots can be clearly observed, while for the [001] direction, horizontal domain structures and spots can be obviously seen which are shown by white arrows in the SAED pattern [inset of Fig. 4(b)]. Such $\frac{1}{2}$ reflection spots are remarkably invisible or extremely weak in the BCZT(1T) film as shown in the tetragonal SAED pattern in Fig. 4(c) inset, further suggesting the decreasing oxygen nanodomains in the high oxygen pressure grown sample.

B. Low-temperature structural analysis

Figures 5(a) and 5(b) show the temperature dependent XRD θ-2θ scans for BCZT(0.1T) and BCZT(1T), respectively, near the BCZT (*002*) plane along with STO (*200*) and LSMO (*200*) peaks, measured from 300 to 30 K at regular intervals of 10 K. The STO (*200*) peaks are separated into two peaks for contributions coming from Cu-$K_{\alpha 1}$ and -$K_{\alpha 2}$ lines. There is a continuous shift of the BCZT (*002*) peak position towards a higher 2θ value with the increase of temperature [as shown in the insets to Figs. 5(a) and 5(b)]. Figures 5(c) and 5(d) show the temperature dependence of the out-of-plane lattice parameter [$c(T)$] for BCZT(0.1T) and BCZT(1T) films, respectively, in the temperature range from 300 to 30 K, as calculated from the XRD scans in Figs. 5(a) and 5(b). From Fig. 5(c), a sharp change in the slope of the $c(T)$ versus T plot can be observed at around 160 K temperature for BCZT(0.1T) film. On the other hand, the change in slope of the $c(T)$ versus T plot observed around 164 K for BCZT(1T) in Fig. 5(d) is quite gradual as compared to the BCZT(0.1T) film. Since the observed changes in the temperature dependence of the lattice parameters for the BCZT(0.1T) and BCZT(1T) films in Figs. 5(c) and 5(d) are quite small in magnitude; they could possibly indicate local structure changes and may not necessarily be attributed to structural phase transition in the relaxor BCZT films, as previously reported in the lead-based relaxors [20,91]. Previously from XRD analyses [Fig. 2(d)], we had seen that BCZT(0.1T) thin film exhibited higher tetragonality

than BCZT(1T) at room temperature. This higher tetragonality in BCZT(0.1T) thin film possibly leads to the anomalous change in lattice parameter at a slightly lower temperature than BCZT(1T) thin film. The out-of-plane lattice parameters at 300 K for the BCZT(0.1T) and BCZT(1T) in Figs. 5(c) and 5(d) matches the same calculated from the room-temperature XRD scans in Fig. 1(b) which affirms that the BCZT (*001*) films are tetragonal at 300 K. To our knowledge, the observation of the low-temperature structural transition has not yet been evidenced in epitaxial BCZT thin films, possibly due to the challenges in detecting the extremely small degree of distortion in the BCZT unit cell above and below the transition temperature along with the presence of strong twinning in the lattice. Since the polarization direction of the tetragonal
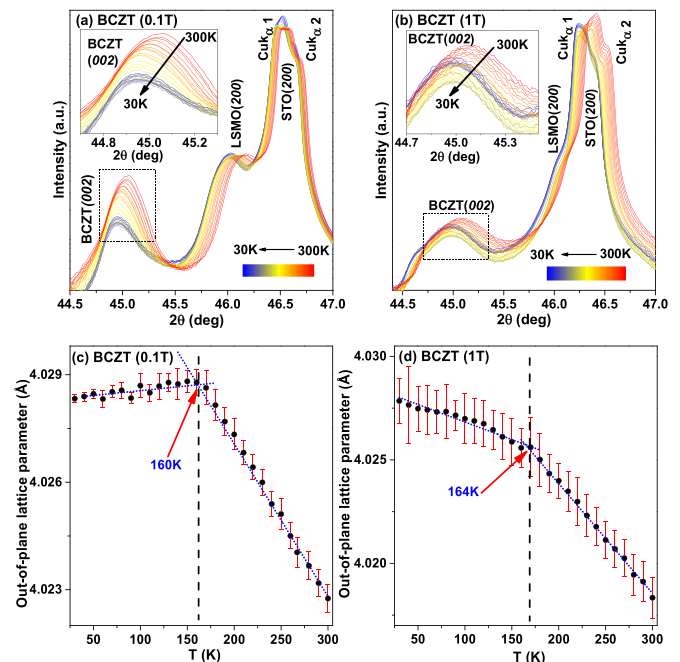

FIG. 5. Temperature dependent XRD θ-2θ scans performed about the BCZT (*002*) plane from 300 to 30 K for (a) BCZT(0.1T) and (b) BCZT(1T) thin films, respectively. Insets to (a) and (b) show the close-up view of the temperature evolution of the BCZT (002) peaks. Out-of-plane lattice parameter (*c*) for the BCZT unit cell at different temperatures calculated from the XRD patterns in (a) and (b) for (c) BCZT(0.1T) and (d) BCZT(1T) thin films, respectively.
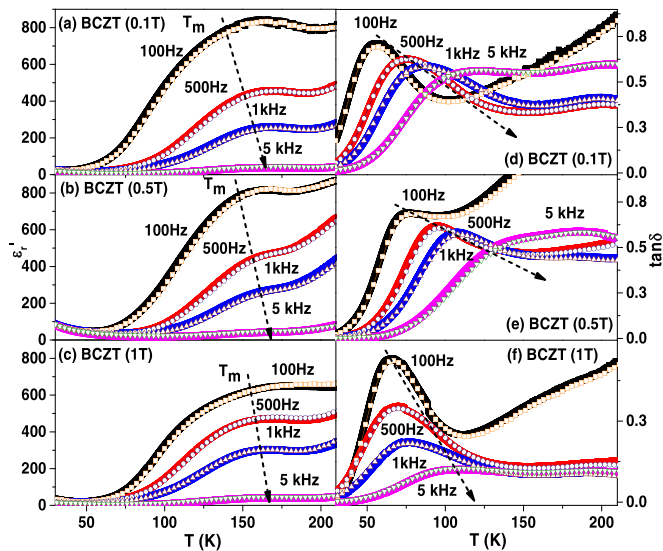
FIG. 6. Temperature dependent (a)–(c) dielectric constant (ε_r') and (d)–(f) dielectric loss (tanδ) for BCZT(0.1T), BCZT(0.5T), and BCZT(1T) thin films measured during heating (open symbols) and cooling cycles (closed symbols), respectively.

BCZT structure coincides with one of the three original cubic [*100*] directions, it is difficult to resolve the structural change using XRD [92].

C. Low-temperature dielectric properties

Figure 6 shows the temperature dependence of the (a)–(c) dielectric constant ε_r' and (d)–(f) dielectric loss, tanδ for the BCZT(0.1T), BCZT(0.5T), and BCZT(1T) thin films during heating (open symbols) and cooling (closed symbols) cycles at 100 Hz, 500 Hz, 1 kHz, and 5 kHz frequencies, respectively. From Fig. 6, it is clearly observed that all the $\varepsilon_r'(T)$ curves show broad transition peaks at all frequencies with negligible thermal hysteresis as evident in the heating and cooling curves. The negligible thermal hysteresis loss observed in these BCZT films make them attractive for applications requiring thermal recycling such as in *electrocalorics* [4]. At the same time, the broad transition peaks increase the operating temperature regime of capacitive and electrocaloric devices as compared to materials undergoing first order phase transitions [4]. The generic feature of relaxors, which is a broad maximum in the temperature dependence of the dielectric permittivity, whose position T_m is shifted to higher temperatures as the frequency of the probing field increases, is clearly evident in the $\varepsilon_r'(T)$ curves in Figs. 6(a)–6(c) in the BCZT (*001*) thin films [8,15]. The dielectric maxima temperature (T_m) [as determined from the $(d\varepsilon_r'/dT)$ vs T plots at different frequencies, shown in the Supplemental Material [67] (Fig. S4)], where the maximum dielectric constant ($\varepsilon_{r\text{max}}'$) is observed in the $\varepsilon_r'(T)$ curves in Figs. 6(a)–6(c) for the BCZT(0.1T), BCZT(0.5T), and BCZT(1T) films, have been listed in Table I. As evident from Figs. 6(a)–6(c) and Table I, the maximum value of ε_r' decrease systematically with increasing P_{O_2}. This observation is also corroborated from the temperature dependence of real part of impedance (Z') for the BCZT thin films plotted at different frequencies as

shown in the Supplemental Material [67] (Fig. S5). For the BCZT(0.1T) film, due to the presence of a large number of V_O resulting in a higher concentration of free charge carriers, there is a lower impedance value ($Z' \sim 8\,\text{M}\Omega$ at 100 Hz) as compared to BCZT(0.5T) ($Z' \sim 20\,\text{M}\Omega$ at 100 Hz) and BCZT(1T) ($Z' \sim 40\,\text{M}\Omega$ at 100 Hz). From Figs. 6(a)–6(c) it is observed that the T_m values increase and shift towards higher temperatures at increasing frequencies (as shown by the dotted arrow). The tanδ plots also show a maximum at T_m, which increases with the increasing frequency. The tanδ value is higher for the film grown at lower P_{O_2} because of higher leakage current as shown in the Supplemental Material [67] (Fig. S6). From the Supplemental Material [67] (Fig. S6), it is observed that the leakage current density decreased systematically from BCZT(0.1T) to BCZT(1T) as the P_{O_2} is increased from 0.1 to 1 Torr, which indicates a reduced concentration of V_O and the associated charged carriers within the films at higher P_{O_2} conditions. In these perovskite thin films, the V_O's behave like donor-type charge carriers providing extra electrons in the conduction band acting as free charge carriers, thus participating in current conduction and increasing the leakage current [76]. The free charge carrier formation can be estimated as follows [93]:

$$\text{O}_O \rightarrow \tfrac{1}{2}\text{O}_2 + V_O^{2+} + 2e^-, \tag{1}$$
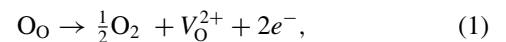
where, O_O is oxygen ion at its normal site and V_O is the oxygen vacancy. It has been theoretically postulated that the V_O's could be located nearer to the Ti/Zr (B site) ions in the perovskite BCZT (ABO_3-type) structure forming dipolar defects (V_O-Ti/Zr) that could generate a local polar distortion and possibly create dipolar clusters within the films [53,94,95]. Hence, the complex frequency dependent diffused dielectric response might possibly be attributed to the formation of dipolar clusters composed of V_O-mediated dipolar defects in the BCZT thin films. The degree of diffusiveness (D') of the dielectric transition can be measured using the following equation [96]:

$$D' = T_{(d\varepsilon_r'/dT)_{\text{min}}} - T_{(d\varepsilon_r'/dT)_{\text{max}}}, \tag{2}$$

where $T_{(d\varepsilon_r'/dT)_{\text{max}}}$ and $T_{(d\varepsilon_r'/dT)_{\text{min}}}$ represent the temperature of the minima and maxima of $(d\varepsilon_r'/dT)$ versus T curves as shown in the Supplemental Material [67] (Fig. S4). Table I lists the calculated D' values for the BCZT thin films at 1 kHz frequency. It is revealed that the D' value is largest for BCZT(1T) thin film and smallest for BCZT(0.1T) thin film. The frequency dispersion phenomena, high leakage current at low P_{O_2}, and diffuse transitions as observed in the BCZT (*001*) films grown under varying P_{O_2} conditions give insight to a dielectric anomaly due to the formation of dipolar clusters associated with V_O-induced defect dipoles. The relaxor nature in the BCZT (*001*) films is confirmed by fitting the frequency dependence of T_m using the Vogel-Fulcher relationship in Eq. (3) as previously reported for low-temperature dielectric relaxation in perovskite [97] and in relaxor BCZT thin films [47–49]:

$$f = f_0 e^{-E_a/k_B(T_m - T_{\text{VF}})}, \tag{3}$$

where E_a is the activation energy, k_B is the Boltzmann constant, T_{VF} is the Vogel-Fulcher freezing temperature, and f_0
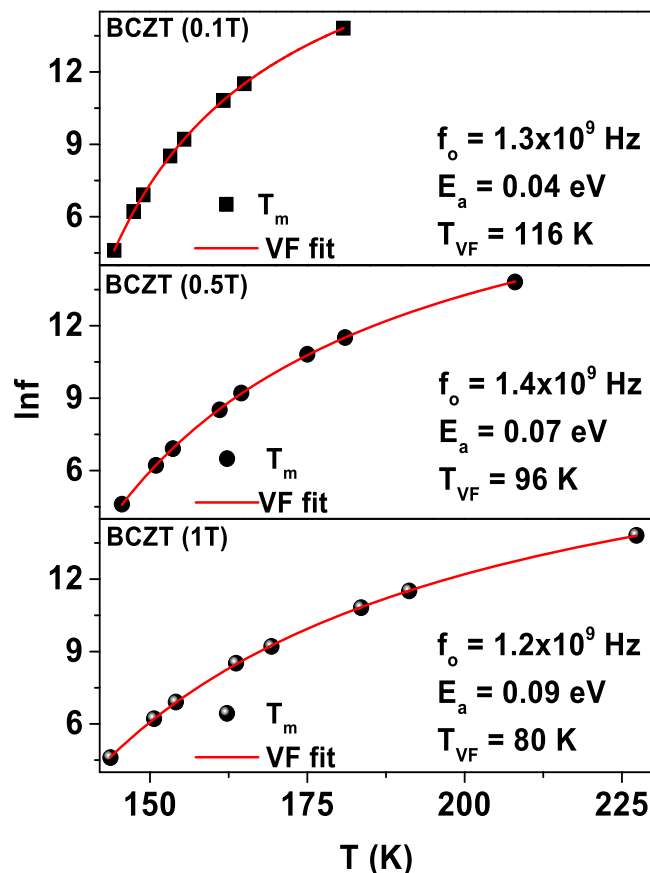
FIG. 7. (a)–(c) $\ln f$ versus T plot with Vogel-Fulcher fitting for BCZT(0.1T), BCZT(0.5T), and BCZT(1T), respectively.

is an attempt frequency. Figures 7(a)–7(c) show the $\ln f$ vs T plots with the Vogel-Fulcher fitting for the BCZT(0.1T), BCZT(0.5T), and BCZT(1T) films, respectively. It is noted that the Vogel-Fulcher fitting in Fig. 7 has been performed across a wide range of frequencies from 100 Hz to 1 MHz [see Fig. S7 in the Supplemental Material [67] for the $\varepsilon'_r(T)$ curves]. From Fig. 7 it is evident that there is a very close match of the experimental data of the frequency dependence of T_m with the Vogel-Fulcher fitting which validates the freezing behavior of dipolar clusters in the BCZT (*001*) thin films [53]. The fitting parameters used in the Vogel-Fulcher relation are summarized in Table I. From the figure and Table I, it is clearly observed that while f_0 remains the same, there is a systematic increase in E_a and a corresponding decrease in T_{VF} in the BCZT (*001*) films with the decrease of V_O concentrations. In fact, the Vogel-Fulcher fitting parameters for the BCZT(1T) film ($f_0 = 1 \times 10^9$ Hz, $T_{VF} = 80$ K) are very close to that of V_O-deficient BaTiO$_3$ single crystal ($f_0 = 4 \times 10^9$ Hz, $T_{VF} = 78$ K); which possibly implies a similar mechanism of dipolar relaxation in these systems at low V_O concentrations [45]. However, the increase in T_{VF} to higher temperatures and the decrease in E_a values in the BCZT(0.5T) and BCZT(0.1T) films indicate that the dielectric relaxations are strongly influenced by increasing V_O concentrations. This observation directly corroborates with the predictions of the recent theoretical

models on V_O-induced dielectric relaxation in traditional FE perovskites [53,60,98].

D. Mechanisms and modeling

In support of the experimental understanding and conclusions, a mechanistic model is proposed to explain the role of V_O in the dielectric relaxor behavior in our BCZT (*001*) thin films. First, we consider the tetragonal perovskite BCZT unit cell with no V_O related defects as schematically shown in Fig. 8(a). Within the oxygen octahedral, the Ti^{4+}/Zr^{4+} ions (*B* site) are noncentrosymmetric which causes a spontaneous dipole moment along the [*001*] direction as shown by blue arrow in Fig. 8(a). Here, we consider that the spontaneous polarization is directed along the out-of-plane direction and proportional to the degree of tetragonality which decreases with lower V_O concentrations in our BCZT (*001*) films (see Table I) [13]. Recently, the existence of out-of-plane-oriented V_O dipoles was experimentally established in strained epitaxial BaTiO$_3$ (*001*) thin films by analyses of the crystal and electronic structure as well as the ferroelectric and optical properties [99]. The formation of the defects was shown to occur in the presence of in-plane compressive strain and oxygen-deficient deposition conditions [99]. The in-plane compressive strain was suggested to favor the formation of V'_Os in the Ba-O planes and thus stabilize the out-of-plane orientation of the dipolar $(V_O^{+2} - \text{Ti}^{3+})^+$ defects [58,99]. Considering this we assign the location of V_O within the BCZT unit cell also to be along the [*001*] direction [as shown in Fig. 8(b)] in our epitaxial BCZT (*001*) thin films deposited under varying P_{O_2} conditions and exhibiting in-plane compressive strains. This is also evidenced in the HRTEM images in Fig. 4 where the V_O defects are located along the [*001*] direction [58,99]. The [*001*] orientation of the V'_Os in the BCZT lattice possibly gives rise to (V_O-Ti/Zr) defect dipoles also oriented along the [*001*] direction [as shown by yellow arrows in Fig. 8(b)] similar to that reported in the epitaxial BaTiO$_3$ (*001*) thin film [99]. The ionic radius of the O^{2-} (1.40 Å) and so its vacancy (V_O) is much larger than the ionic radii of Zr^{4+} (0.72 Å) and Ti^{4+} (0.67 Å) and slightly larger than that of Ba^{2+} (1.35 Å) and Ca^{2+} (1.34 Å) in the BCZT structure; hence, it is considered that the off-centering of the Ti^{4+}/Zr^{4+} ions in the tetragonal BCZT lattice does not affect the position of V_O [see Fig. 8(b)], as previously reported in the V_O-mediated lead-based perovskites [100]. The dipolar clusters composed of such clustered V_O-related defect dipoles could possibly govern the relaxor behavior in the BCZT thin films. For the BCZT(0.1T) film [shown schematically in Fig. 8(c)], having a higher concentration of V_O, the defect dipoles (V_O-Ti/Zr) interact with close neighboring defect dipoles to form large dipolar clusters of polar relaxor states [as shown by yellow color circles in Fig. 8(c)], as also observed in other FE relaxors [60,74,75,101]. The polar vectors of these dipolar clusters are proposed to be oriented "collinear" with the [*001*] polar direction (shown by the blue arrow) of the FE matrix in the BCZT (*001*) films. Thus, a coexistence of the polar FE states and relaxor states can be realized in the BCZT(0.1T) film [53]. Based on the calculations of oxygen deficiency using XPS analyses (Table I), we postulate that the percentage of V_O in the BCZT thin films
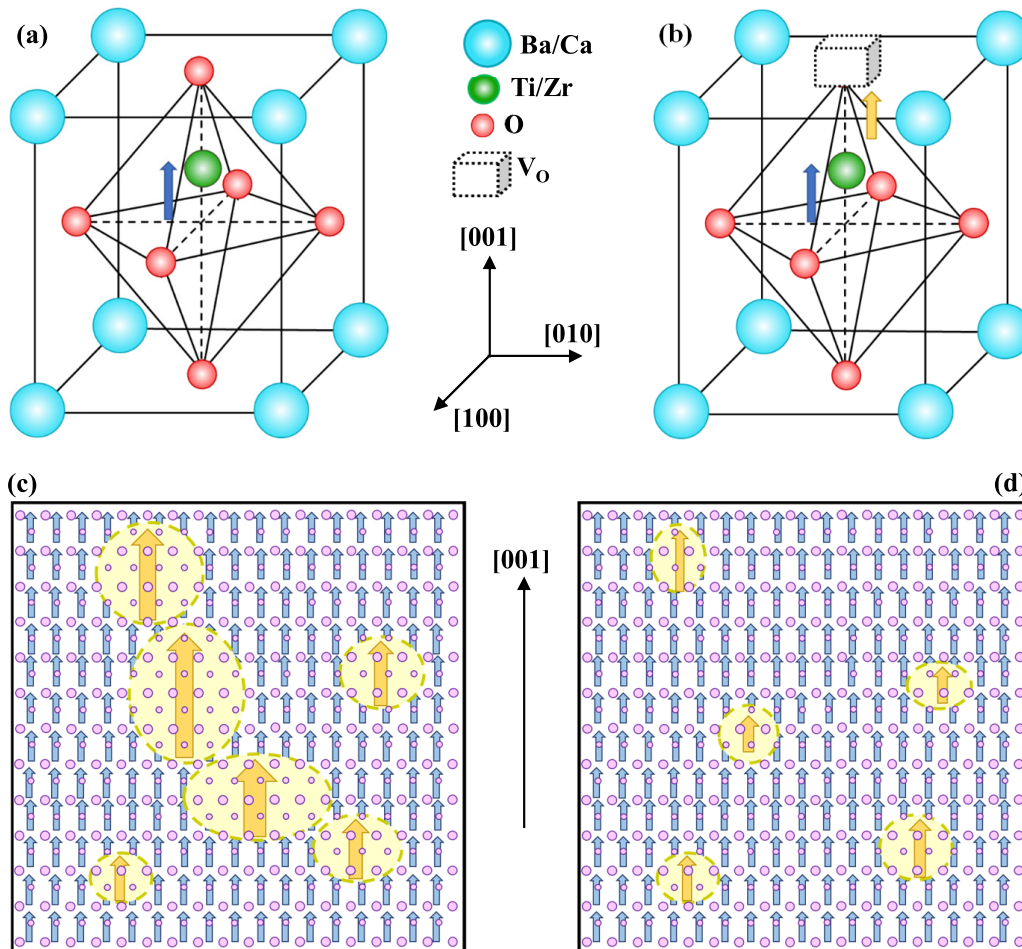
FIG. 8. (a),(b) Schematic diagrams of the tetragonal BCZT unit cell in the absence and presence of an oxygen vacancy (V_O), respectively. The spontaneous polarization and the V_O induced defect dipole are shown by blue and yellow arrows, respectively. (c),(d) Schematic diagrams of dipolar-cluster formation in BCZT thin films under high and low concentrations of oxygen vacancies, respectively. The yellow circles represent the collinear dipolar-clusters coexisting in the FE matrix whose polarization directions is denoted by the blue arrow in the BCZT (*001*) thin films as shown by the upward arrow along the [*001*] direction.

which give rise to stable dipolar-cluster formation and the observed dielectric relaxation behavior vary from 9% in the BCZT(0.1T) film to 6% in the BCZT(0.5T) film to as low as 2% in the BCZT(1T) film, respectively. On the other hand, for the BCZT(1T) film [shown schematically in Fig. 8(d)], having lower V_O concentration, the V_O-related collinear dipolar clusters have less overlap interaction which limits large dipolar-cluster formations. Li *et al.* reported that it is energetically more favorable to reorient the strongly interacting large dipolar clusters as in BCZT(0.1T) film [Fig. 8(c)] than the weakly interacting dipolar clusters in BCZT(1T) film [Fig. 8(d)]; the activation energy for the dipolar-clusters in BCZT(0.1T) film is lower than that of the BCZT(1T) film as shown in Table I [20]. This is consistent with the phenomenological theoretical model predicted by Glinchuk *et al.* for V_O-induced relaxor behavior in the perovskite structure [53]. The relaxor behavior observed in our BCZT films is enhanced near the low-temperature dielectric transition where the effects of free charge carriers are not that dominant, but the localized defect dipoles forming the dipolar clusters give rise to the relaxor behavior in the dielectric dispersion as

reported here in the BCZT thin films grown under varying P_{O_2} conditions.

IV. CONCLUSIONS

In summary, BCZT/LSMO thin film heterostructures were fabricated using PLD technique on single crystal STO (*100*) substrates at different P_{O_2} from 0.1 to 1 Torr. The varying V_O concentrations in the BCZT films gave rise to a systematic tuning of the tetragonality in the BCZT films as evidenced from XRD analysis. XPS analysis showed that (Ti + Zr)/(Ba + Ca) cationic occupancy ratio increased while the percentage of V_O per unit cell decreased with increasing P_{O_2}. Low-temperature XRD analyses revealed a change in the lattice parameter at 160 and 164 K for BCZT(0.1T) and BCZT(1T), respectively. Low-temperature dielectric measurements showed evidence of relaxor behavior with diffuse transitions. Vogel-Fulcher fitting of dielectric dispersion and T_m confirmed the relaxor behavior of the thin films and revealed that the activation energy of the dipolar clusters formed due to V_O-induced defects increases with increasing P_{O_2}, as

evidenced by HRTEM. We propose that the low-temperature dielectric relaxations observed in the BCZT thin films deposited under varying P_{O_2} conditions are strongly affected due to the presence of clustered V_O-induced dipolar defects. The work provides a fundamental understanding of the relaxor behavior and the tunability of the low-temperature dielectric properties through variation of the V_O concentration in lead-free BCZT thin films.

The data that support the findings of this study are available from the corresponding authors upon reasonable request.

[1] A. A. Bokov and Z. G. Ye, Recent progress in relaxor ferroelectrics with perovskite structure, J. Mater. Sci. **41**, 31 (2006).

[2] R. A. Cowley, S. N. Gvasaliya, S. G. Lushnikov, B. Roessli, and G. M. Rotaru, Relaxing with relaxors: A review of relaxor ferroelectrics, Adv. Phys. **60**, 229 (2011).

[3] L. E. Cross, Relaxor ferroelectrics: an overview, Ferroelectrics **151**, 305 (1994).

[4] A. Barman, S. Kar-Narayan, and D. Mukherjee, Caloric effects in perovskite oxides, Adv. Mater. Interfaces **6**, 1900291 (2019).

[5] A. Datta, D. Mukherjee, and S. Kar-Narayan, Ferroelectric and piezoelectric oxide nanostructured films for energy harvesting applications, in *Metal Oxide-Based Thin Film Structures*, edited by N. Pryds and V. Esposito (Elsevier, Amsterdam, 2018), pp. 465–488.

[6] P. Zhao, H. Wang, L. Wu, L. Chen, Z. Cai, L. Li, and X. Wang, High-performance relaxor ferroelectric materials for energy storage applications, Adv. Energy Mater. **9**, 1803048 (2019).

[7] L. Yang, X. Kong, F. Li, H. Hao, Z. Cheng, H. Liu, J. F. Li, and S. Zhang, Perovskite lead-free dielectrics for energy storage applications, Prog. Mater. Sci. **102**, 72 (2019).

[8] V. V. Shvartsman and D. C. Lupascu, Lead-free relaxor ferroelectrics, J. Am. Ceram. Soc. **95**, 1 (2012).

[9] J. Rödel, W. Jo, K. T. P. Seifert, E. M. Anton, T. Granzow, and D. Damjanovic, Perspective on the development of lead-free piezoceramics, J. Am. Ceram. Soc. **92**, 1153 (2009).

[10] C. W. Ahn, C. H. Hong, B. Y. Choi, H. P. Kim, H. S. Han, Y. Hwang, W. Jo, K. Wang, J. F. Li, J. S. Lee, and I. W. Kim, A brief review on relaxor ferroelectrics and selected issues in lead-free relaxors, J. Korean Phys. Soc. **68**, 1481 (2016).

[11] A. Kursumovic, W. W. Li, S. Cho, P. J. Curran, D. H. L. Tjhe, and J. L. MacManus-Driscoll, Lead-free relaxor thin films with huge energy density and low loss for high temperature applications, Nano Energy **71**, 104536 (2020).

[12] A. P. Sharma, M. K. Behera, D. K. Pradhan, S. K. Pradhan, C. E. Bonner, and M. Bahoura, Lead-free relaxor-ferroelectric thin films for energy harvesting from low-grade waste-heat, Sci. Rep. **11**, 111 (2021).

[13] A. Barman, S. Chatterjee, C. Ou, Y. Yau Tse, N. Banerjee, S. Kar-Narayan, A. Datta, and D. Mukherjee, Large electrocaloric effect in lead-free ferroelectric $Ba_{0.85}Ca_{0.15}Ti_{0.9}Zr_{0.1}O_3$ thin film heterostructure, APL Mater. **9**, 021115 (2021).

[14] H. Pan, F. Li, Y. Liu, Q. Zhang, M. Wang, S. Lan, Y. Zheng, J. Ma, L. Gu, Y. Shen, P. Yu, S. Zhang, L. Q. Chen, Y. H. Lin, and C. W. Nan, Ultrahigh–energy density lead-free dielectric films via polymorphic nanodomain design, Science **365**, 578 (2019).

[15] S. Pandya, J. Wilbur, J. Kim, R. Gao, A. Dasgupta, C. Dames, and L. W. Martin, Pyroelectric energy conversion with large energy and power density in relaxor ferroelectric thin films, Nat. Mater. **17**, 432 (2018).

[16] L. L. Zhang and Y. N. Huang, Theory of relaxor-ferroelectricity, Sci. Rep. **10**, 5060 (2020).

[17] M. J. Krogstad, P. M. Gehring, S. Rosenkranz, R. Osborn, F. Ye, Y. Liu, J. P. C. Ruff, W. Chen, J. M. Wozniak, H. Luo, O. Chmaissem, Z. G. Ye, and D. Phelan, The relation of local order to material properties in relaxor ferroelectrics, Nat. Mater. **17**, 718 (2018).

[18] H. Takenaka, I. Grinberg, S. Liu, and A. M. Rappe, Slush-like polar structures in single-crystal relaxors, Nature (London) **546**, 391 (2017).

[19] I. K. Jeong, T. W. Darling, J. K. Lee, T. Proffen, R. H. Heffner, J. S. Park, K. S. Hong, W. Dmowski, and T. Egami, Direct Observation of the Formation of Polar Nanoregions in $Pb(Mg_{1/3}Nb_{2/3})O_3$ Using Neutron Pair Distribution Function Analysis, Phys. Rev. Lett. **94**, 147602 (2005).

[20] F. Li, S. Zhang, T. Yang, Z. Xu, N. Zhang, G. Liu, J. Wang, J. Wang, Z. Cheng, Z. G. Ye, J. Luo, T. R. Shrout, and L. Q. Chen, The origin of ultrahigh piezoelectricity in relaxor-ferroelectric solid solution crystals, Nat. Commun. **7**, 13807 (2016).

[21] M. Eremenko, V. Krayzman, A. Bosak, H. Y. Playford, K. W. Chapman, J. C. Woicik, B. Ravel, and I. Levin, Local atomic order and hierarchical polar nanoregions in a classical relaxor ferroelectric, Nat. Commun. **10**, 2728 (2019).

[22] D. Damjanovic, A. Biancoli, L. Batooli, A. Vahabzadeh, and J. Trodahl, Elastic, dielectric, and piezoelectric anomalies and raman spectroscopy of $0,5Ba(Ti_{0.8}Zr_{0.2})O_3$-$0.5(Ba_{0.7}Ca_{0.3})TiO_3$, Appl. Phys. Lett. **100**, 192907 (2012).

[23] A. Datta P. E. Sanchez-Jimenez, R. A. R. A. Orabi, Y. Calahorra, C. Ou, S. Sahonta, M. Fornari, and S. Kar-Narayan, Lead-free polycrystalline ferroelectric nanowires with enhanced curie temperature, Adv. Funct. Mater **27**, 1701169 (2017).

[24] Z. Hanani, D. Mezzane, M. Amjoud, A. G. Razumnaya, S. Fourcade, Y. Gagou, K. Hoummada, M. El Marssi, and M. Gouné, Phase transitions, energy storage performances and electrocaloric effect of the lead-free $Ba_{0.85}Ca_{0.15}Zr_{0.10}Ti_{0.90}O_3$ ceramic relaxor, J. Mater. Sci. Mater. Electron. **30**, 6430 (2019).

[25] J. Hao, W. Bai, W. Li, and J. Zhai, Correlation between the microstructure and electrical properties in high-performance $(Ba_{0.85}Ca_{0.15})(Zr_{0.1}Ti_{0.9})$ O_3 lead-free piezoelectric ceramics, J. Am. Ceram. Soc. **95**, 1998 (2012).

[26] W. Liu and X. Ren, Large Piezoelectric Effect in Pb-Free Ceramics, Phys. Rev. Lett. **103**, 257602 (2009).

[27] A. P. Turygin, M. M. Neradovskiy, N. A. Naumova, D. V. Zayats, I. Coondoo, A. L. Kholkin, and V. Y. Shur, Domain structures and local switching in lead-free piezoceramics $Ba_{0.85}Ca_{0.15}Ti_{0.90}Zr_{0.10}O_3$, J. Appl. Phys. **118**, 072002 (2015).

[28] Y. Tian, L. Wei, X. Chao, Z. Liu, and Z. Yang, Phase transition behavior and large piezoelectricity near the morphotropic phase boundary of lead-free $(Ba_{0.85}Ca_{0.15})(Zr_{0.1}Ti_{0.9})O_3$ ceramics, J. Am. Ceram. Soc. **96**, 496 (2013).

[29] M. Acosta, N. Novak, W. Jo, and J. Rödel, Relationship between electromechanical properties and phase diagram in the $Ba(Zr_{0.2}Ti_{0.8})O_{3-x}(Ba_{0.7}Ca_{0.3})TiO_3$ lead-free piezoceramic, Acta Mater. **80**, 48 (2014).

[30] J. P. B. Silva, E. C. Queirós, P. B. Tavares, K. C. Sekhar, K. Kamakshi, J. A. Moreira, A. Almeida, M. Pereira, and M. J. M. Gomes, Ferroelectric phase transitions studies in $0.5Ba(Zr_{0.2}Ti_{0.8})O_3$-$0.5(Ba_{0.7}Ca_{0.3})TiO_3$ ceramics, J. Electroceram. **35**, 135 (2015).

[31] J. P. Praveen, T. Karthik, A. R. James, E. Chandrakala, S. Asthana, and D. Das, Effect of poling process on piezoelectric properties of sol-gel derived BZT-BCT ceramics, J. Eur. Ceram. Soc. **35**, 1785 (2015).

[32] V. R. Mastelaro, H. R. Favarim, A. Mesquita, A. Michalowicz, J. Moscovici, and J. A. Eiras, Local structure and hybridization states in $Ba_{0.9}Ca_{0.1}Ti_{1-x}Zr_xO_3$ ceramic compounds: Correlation with a normal or relaxor ferroelectric character, Acta Mater. **84**, 164 (2015).

[33] H. Kaddoussi, Y. Gagou, A. Lahmar, J. Belhadi, B. Allouche, J.-L. Dellis, M. Courty, H. Khemakhem, and M. El Marssi, Room temperature electro-caloric effect in lead-free $Ba(Zr_{0.1}Ti_{0.9})1 - xSn_xO_3$ ($x = 0$, $x = 0.075$) ceramics, Solid State Commun. **201**, 64 (2015).

[34] M. Kumar, A. Garg, R. Kumar, and M. C. Bhatnagar, Structural, dielectric and ferroelectric study of $Ba_{0.9}Sr_{0.1}Zr_xTi_{1-x}O_3$ ceramics prepared by the sol–gel method, Phys. B (Amsterdam, Neth.) **403**, 1819 (2008).

[35] Z. Yu, R. Guo, and A. S. Bhalla, Orientation dependence of the ferroelectric and piezoelectric behavior of $Ba(Ti_{1-x}Zr_x)O_3$ single crystals, Appl. Phys. Lett. **77**, 1535 (2000).

[36] Z. Yu, C. Ang, R. Guo, and A. S. Bhalla, Piezoelectric and strain properties of $Ba(Ti_{1-x}Zr_x)O_3$ Ceramics, J. Appl. Phys. **92**, 1489 (2002).

[37] A. K. Kalyani, A. Senyshyn, and R. Ranjan, Polymorphic phase boundaries and enhanced piezoelectric response in extended composition range in the lead free ferroelectric $BaTi_{1-x}Zr_xO_3$, J. Appl. Phys. **114**, 014102 (2013).

[38] I.-K. Jeong and J. S. Ahn, The atomic structure of lead-free $Ba(Zr_{0.2}Ti_{0.8})O_3$-$(Ba_{0.7}Ca_{0.3})TiO_3$ by using neutron total scattering analysis, Appl. Phys. Lett. **101**, 242901 (2012).

[39] D. S. Keeble, F. Benabdallah, P. A. Thomas, M. Maglione, and J. Kreisel, Revised structural phase diagram of $(Ba_{0.7}Ca_{0.3}TiO_3)$-$(BaZr_{0.2}Ti_{0.8}O_3)$, Appl. Phys. Lett. **102**, 092903 (2013).

[40] I. Levin, V. Krayzman, and J. C. Woicik, Local-structure origins of the sustained Curie temperature in $(Ba,Ca)TiO_3$ ferroelectrics, Appl. Phys. Lett. **102**, 162906 (2013).

[41] Y. Tian, X. Chao, L. Jin, L. Wei, P. Liang, and Z. Yang, Polymorphic structure evolution and large piezoelectric response of lead-free $(Ba,Ca)(Zr,Ti)O_3$ ceramics, Appl. Phys. Lett. **104**, 112901 (2014).

[42] X.-G. Tang and H. L.-W. Chan, Effect of grain size on the electrical properties of $(Ba,Ca)(Zr,Ti)O_3$ relaxor ferroelectric ceramics, J. Appl. Phys. **97**, 034109 (2005).

[43] R. Comes, M. Lambert, and A. Guinier, The chain structure of $BaTiO_3$ and $KNbO_3$, Solid State Commun. **6**, 715 (1968).

[44] Y. Akishige, T. Nakanishi, and N. Mori, Dielectric dispersion in BaTiO3 single crystal at low temperatures, Ferroelectrics **217**, 217 (1998).

[45] Y. Akishige and N. Mori, Low temperature dielectric dispersion in $BaTiO_3$ single crystal, J. Korean Phys. Soc. **35**, S1441 (1999).

[46] K. Tsuda, R. Sano, and M. Tanaka, Nanoscale local structures of rhombohedral symmetry in the orthorhombic and tetragonal phases of $BaTiO_3$ studied by convergent-beam electron diffraction, Phys. Rev. B **86**, 214106 (2012).

[47] Y. Lin, N. Qin, G. Wu, T. Sa, and D. Bao, Dielectric relaxor behaviors and tenability of $(1 - x)Ba(Zr_{0.2}Ti_{0.8})O_3$-$x(Ba_{0.7}Ca_{0.3})TiO_3$ thin films fabricated by sol-gel method, Appl. Phys. A: Mater. Sci. Process. **109**, 743 (2012).

[48] C. Bhardwaj, B. S. S. Daniel, and D. Kaur, Pulsed laser deposition and characterization of highly tunable (1-x)$Ba(Zr_{0.2}Ti_{0.8})O_3$-x$(Ba_{0.7}Ca_{0.3})TiO_3$ thin films grown on $LaNiO_3$/Si substrate, J. Phys. Chem. Solids **74**, 94 (2013).

[49] A. Piorra, V. Hrkac, N. Wolff, C. Zamponi, V. Duppel, J. Hadermann, L. Kienle, and E. Quandt, $(Ba_{0.85}Ca_{0.15})(Ti_{0.9}Zr_{0.1})O_3$ thin films prepared by PLD: Relaxor properties and complex microstructure, J. Appl. Phys. **125**, 244103 (2019).

[50] J. P. B. Silva, K. Kamakshi, R. F. Negrea, C. Ghica, J. Wang, G. Koster, G. Rijnders, F. Figueiras, M. Pereira, and M. J. M. Gomes, Ferroelectric switching dynamics in $0.5Ba(Zr_{0.2}Ti_{0.8})O_3$-$0.5(Ba_{0.7}Ca_{0.3})TiO_3$ thin films, Appl. Phys. Lett. **113**, 082903 (2018).

[51] M. Hu, S. Li, and C. Wang, Epitaxial growth and multiferroic properties of artificial LCMO/BCZT heterostructure on (100) MgO substrate by pulsed laser deposition, J. Phys. D: Appl. Phys. **53**, 015002 (2020).

[52] S. E. Shirsath, C. Cazorla, T. Lu, L. Zhang, Y. Y. Tay, X. Lou, Y. Liu, S. Li, and D. Wang, Interface-charge induced giant electrocaloric effect in lead free ferroelectric thin-film bilayers, Nano Lett. **20**, 1262 (2020).

[53] M. D. Glinchuk, E. A. Eliseev, G. Li, J. Zeng, S. V Kalinin, and A. N. Morozovska, Ferroelectricity induced by oxygen

vacancies in relaxors with perovskite structure, Phys. Rev. B **98**, 094102 (2018).

[54] G. Deng, G. Li, A. Ding, and Q. Yin, Evidence for oxygen vacancy inducing spontaneous normal-relaxor transition in complex perovskite ferroelectrics, Appl. Phys. Lett. **87**, 192905 (2005).

[55] J. F. Scott and M. Dawber, Oxygen-vacancy ordering as a fatigue mechanism in perovskite ferroelectrics, Appl. Phys. Lett. **76**, 3801 (2000).

[56] W. Li, K. Chen, Y. Y. Yao, Ji. S. Zhu, and Y. N. Wang, Correlation among oxygen vacancies in bismuth titanate ferroelectric ceramics, Appl. Phys. Lett. **85**, 4717 (2004).

[57] W. Li, J. Gu, Q. He, K. H. L. Zhang, C. Wang, K. Jin, Y. Wang, M. Acosta, H. Wang, A. Y. Borisevich, J. L. MacManus-Driscoll, and H. Yang, Oxygen-vacancy-mediated dielectric property in perovskite $Eu_{0.5}Ba_{0.5}TiO_{3-\delta}$ epitaxial thin films, Appl. Phys. Lett. **112**, 182906 (2018).

[58] R. A. Maier, T. A. Pomorski, P. M. Lenahan, and C. A. Randall, Acceptor-oxygen vacancy defect dipoles and fully coordinated defect centers in a ferroelectric perovskite lattice: Electron paramagnetic resonance analysis of Mn^{2+} in single crystal $BaTiO_3$, J. Appl. Phys. **118**, 164102 (2015).

[59] L. N. Liu, C. C. Wang, X. H. Sun, G. J. Wang, C. M. Lei, and T. Li, Oxygen-vacancy-related relaxations of $Sr_3CuNb_2O_9$ at high temperatures, J. Alloy. Compd. **552**, 279 (2013).

[60] T. Zhang, X. G. Tang, Q. X. Liu, S. G. Lu, Y. P. Jiang, X. X. Huang, and Q. F. Zhou, Oxygen-vacancy-related relaxation and conduction behavior in $(Pb_{1-x}Ba_x)(Zr_{0.95}Ti_{0.05})O_3$ ceramics, AIP Adv. **4**, 107141 (2014).

[61] C. C. Wang, C. M. Lei, G. J. Wang, X. H. Sun, T. Li, S. G. Huang, H. Wang, and Y. D. Li, Oxygen-vacancy-related dielectric relaxations in $SrTiO_3$ at high temperatures, J. Appl. Phys. **113**, 094103 (2013).

[62] D. Mukherjee, P. Mukherjee, H. Srikanth, and S. Witanachchi, Carrier-mediated interaction of magnetic moments in oxygen vacancy–controlled epitaxial Mn-doped ZnO thin films, J. Appl. Phys. **111**, 07C318 (2012).

[63] T. Zhao, F. Chen, H. Lu, G. Yang, and Z. Chen, Thickness and oxygen pressure dependent structural characteristics of $BaTiO_3$ thin films grown by laser molecular beam epitaxy, J. Appl. Phys. **87**, 7442 (2000).

[64] J. Gonzalo, R. Gómez San Román, J. Perrière, C. N. Afonso, and R. Pérez Casero, Pressure effects during pulsed-laser deposition of barium titanate thin films, Appl. Phys. A **66**, 487 (1998).

[65] S. R. Reddy, V. V. B. Prasad, S. Bysakh, V. Shanker, J. Joardar, and S. K. Roy, Ferroelectric and piezoelectric properties of $Ba_{0.85}Ca_{0.15}Ti_{0.90}Zr_{0.10}O_3$ films in 200 nm thickness range, J. Am. Ceram. Soc. **102**, 1277 (2019).

[66] V. S. Puli, A. Kumar, D. B. Chrisey, M. Tomozawa, J. F. Scott, and R. S. Katiyar, Barium zirconate-titanate/barium calcium-titanate ceramics via sol–gel process: Novel high-energy-density capacitors, J. Phys. D. Appl. Phys. **44**, 395403 (2011).

[67] See Supplemental Material at http://link.aps.org/supplemental/10.1103/PhysRevMaterials.5.064415 for the structure refinement and compositional analyses of the BCZT target, derivatives of the temperature dependent dielectric constant curves, temperature dependence of the real part of impedance, variation of maximum dielectric temperature with

frequency, and leakage currents and dielectric dispersion at higher frequencies for BCZT thin films grown under different ambient oxygen pressures using the PLD technique.

[68] M. ben Abdessalem, A. Aydi, and N. Abdelmoula, Raman scattering, structural, electrical studies and conduction mechanism of $Ba_{0.9}Ca_{0.1}Ti_{0.95}Zr_{0.05}O_3$ ceramic, J. Alloys Compd. **774**, 685 (2019).

[69] P. Bharathi, P. Thomas, and K. B. R. Varma, Piezoelectric properties of individual nanocrystallites of $Ba_{0.85}Ca_{0.15}Zr_{0.1}Ti_{0.9}O_3$ obtained by oxalate precursor route, J. Mater. Chem. C **3**, 4762 (2015).

[70] J. H. Jang, M. S. Phen, A. Gerger, K. S. Jones, J. L. Hansen, A. N. Larsen, and V. Craciun, Structural characterization of strained silicon grown on a SiGe buffer layer, Semicond. Sci. Technol. **23**, 035012 (2008).

[71] D. Mukherjee, N. Bingham, M. Hordagoda, M.-H. Phan, H. Srikanth, S. Witanachchi, and P. Mukherjee, Influence of microstructure and interfacial strain on the magnetic properties of epitaxial $Mn_3O_4/La_{0.7}Sr_{0.3}MnO_3$ layered-composite thin films, J. Appl. Phys. **112**, 083910 (2012).

[72] J. Gazquez, S. Bose, M. Sharma, M. A. Torija, S. J. Pennycook, C. Leighton, and M. Varela, Lattice mismatch accommodation via oxygen vacancy ordering in epitaxial $La_{0.5}Sr_{0.5}CoO_{3-\delta}$ thin films, APL Mater. **1**, 012105 (2013).

[73] C. Li, D. Cui, Y. Zhou, H. Lu, Z. Chen, D. Zhang, and F. Wu, Asymmetric rocking curve study of the crystal structure orientations for $BaTiO_3$ thin films grown by pulsed laser deposition, Appl. Surf. Sci. **136**, 173 (1998).

[74] A. P. Chen, F. Khatkhatay, W. Zhang, C. Jacob, L. Jiao, and H. Wang, Strong oxygen pressure dependence of ferroelectricity in $BaTiO_3/SrRuO_3/SrTiO_3$ epitaxial heterostructures, J. Appl. Phys. **114**, 124101 (2013).

[75] C. L. Li, Z. H. Chen, Y. L. Zhou, and D. F. Cui, Effect of oxygen content on the dielectric and ferroelectric properties of laser-deposited $BaTiO_3$ thin films, J. Phys.: Condens. Matter **13**, 5261 (2001).

[76] Q. Lin, D. Wang, and S. Li, Strong effect of oxygen partial pressure on electrical properties of $0.5Ba(Zr_{0.2}Ti_{0.8})O_3-0.5(Ba_{0.7}Ca_{0.3})TiO_3$ thin films, J. Am. Ceram. Soc. **98**, 2094 (2015).

[77] W. Cai, Q. W. Zhang, C. Zhou, R. L. Gao, F. Q. Wang, G. Chen, X. L. Deng, Z. H. Wang, N. Y. Deng, L. Cheng, and C. L. Fu, Effects of oxygen partial pressure on the electrical properties and phase transitions in (Ba,Ca)(Ti,Zr)O-3 ceramics, J. Mater. Sci. **55**, 9972 (2020).

[78] Q. W. Zhang, W. Cai, C. Zhou, R. C. Xu, S. L. Zhang, Z. D. Li, R. L. Gao, and C. L. Fu, Electric fatigue of BCZT ceramics sintered in different atmospheres, Appl. Phys. A: Mater. Sci. Process. **125**, 759 (2019).

[79] S. P. P. Sadhu, S. Siddabattuni, B. Ponraj, M. Molli, V. S. Muthukumar, and K. B. R. Varma, Enhanced dielectric properties and energy storage density of interface controlled ferroelectric BCZT-epoxy nanocomposites, Compos. Interfaces **24**, 663 (2017).

[80] Q. Ji, L. Bi, J. Zhang, H. Cao, and X. S. Zhao, The role of oxygen vacancies of ABO_3 perovskite oxides in the oxygen reduction reaction, Energy Environ. Sci. **13**, 1408 (2020).

[81] P. Pomyai, D. Munthala, T. Sonklin, R. Supruangnet, H. Nakajima, P. Janphuang, S. M. Dale, J. Glaum,

and S. Pojprapai, Electrical fatigue behavior of Ba$_{0.85}$Ca$_{0.15}$Zr$_{0.1}$Ti$_{0.9}$O$_3$ ceramics under different oxygen concentrations, J. Eur. Cer. Soc. **41**, 2497 (2021).

[82] L. Qiao and X. Bi, Direct observation of oxygen vacancy and its effect on the microstructure, electronic and transport properties of sputtered LaNiO$_{3-\delta}$ films on Si substrates, Thin Solid Films **519**, 943 (2010).

[83] G. Liu, X. Li, Y. Wang, W. Liang, B. Liu, H. Feng, H. Yang, J. Zhang, and J. Sun, Nanoscale domains of ordered oxygen-vacancies in LaCoO$_3$ films, Appl. Surf. Sci. **425**, 121 (2017).

[84] S. Seal, A. Jeyaranjan, C. J. Neal, U. Kumar, T. S. Sakthivel, and D. C. Sayle, Engineered defects in cerium oxides: Tuning chemical reactivity for biomedical, environmental, & energy applications, Nanoscale **12**, 6879 (2020).

[85] B. Liu, Y. Wang, G. Liu, H. Feng, H. Yang, X. Xue, and J. Sun, Tuning the magnetic properties of La$_{0.67}$Sr$_{0.33}$CoO$_{3-\delta}$ films by oxygen pressure, Phys. Rev. B **93**, 094421 (2016).

[86] N. J. Lawrence, J. R. Brewer, L. Wang, T.-S. Wu, J. Wells-Kingsbury, M. M. Ihrig, G. Wang, Y.-L. Soo, W.-N. Mei, and C. L. Cheung, Defect engineering in cubic cerium oxide nanostructures for catalytic oxidation, Nano Lett. **11**, 2666 (2011).

[87] D. C. Grinter, R. Ithnin, C. L. Pang, and G. Thornton, Defect structure of ultrathin ceria films on Pt(111): Atomic views from scanning tunnelling microscopy, J. Phys. Chem. C **114**, 17036 (2010).

[88] F. Esch, S. Fabris, L. Zhou, T. Montini, C. Africh, P. Fornasiero, G. Comelli, and R. Rosei, Chemistry: Electron localization determines defect formation on ceria substrates, Science **309**, 752 (2005).

[89] H. Hojo, T. Mizoguchi, H. Ohta, S. D. Findlay, N. Shibata, T. Yamamoto, and Y. Ikuhara, Atomic structure of a CeO$_2$ grain boundary: The role of oxygen vacancies, Nano Lett. **10**, 4668 (2010).

[90] J. R. Croy, S. Mostafa, J. Liu, Y. Sohn, and B. Roldan Cuenya, Size dependent study of MeOH decomposition over size-selected Pt nanoparticles synthesized via micelle encapsulation, Catal. Lett. **118**, 1 (2007).

[91] B. Dkhil, P. Gemeiner, A. Al-Barakaty, L. Bellaiche, E. Dul'kin, E. Mojaev, and M. Roth, Intermediate temperature scale T_* in lead-based relaxor systems, Phys. Rev. B **80**, 064103 (2009).

[92] Y. Tian, X. Chao, L. Wei, P. Liang, and Z. Yang, Phase transition behavior and electrical properties of lead-free (Ba$_{1-x}$Ca$_x$)(Zr$_{0.1}$Ti$_{0.9}$)O$_3$ piezoelectric ceramics, J. Appl. Phys. **113**, 184107 (2013).

[93] S. R. Reddy, V. V. B. Prasad, S. Bysakh, V. Shanker, N. Hebalkar, and S. K. Roy, Superior energy storage performance and fatigue resistance in ferroelectric BCZT thin films grown in an oxygen-rich atmosphere, J. Mater. Chem. C **7**, 7073 (2019).

[94] X. D. Yan, M. P. Zheng, X. Gao, M. K. Zhu, and Y. D. Hou, High-performance lead-free ferroelectric BZT-BCT and its application in energy fields, J. Mater. Chem. C **8**, 13530 (2020).

[95] X. Jia, J. Jhang, L. Wang, J. Wang, H. Du, Y. Yao, L. Ren, F. Wen, and P. Zheng, Role of oxygen-vacancy in piezoelectric properties and fatigue behavior of (Bi$_{0.5}$Na$_{0.5}$)$_{0.93}$Ba$_{0.07}$Ti$_{1+x}$O$_3$ ceramics, J. Am. Ceram. Soc. **102**, 5203 (2019).

[96] Z. Raddaoui, S. El Kossi, J. Dhahri, N. Abdelmoula, and K. Taibi, Study of diffuse phase transition and relaxor ferroelectric behavior of Ba$_{0.97}$Bi$_{0.02}$Ti$_{0.9}$Zr$_{0.05}$Nb$_{0.04}$O$_3$ Ceramic, RSC Adv. **9**, 2412 (2019).

[97] D. A. Ochoa, R. Levit, C. M. Fancher, G. Esteves, J. L. Jones, and J. E. Garcia, Low temperature dielectric relaxation in ordinary perovskite ferroelectrics: Enlightenment from high-energy x-ray diffraction, J. Phys. D: Appl. Phys. **50**, 205305 (2017).

[98] B. S. Kang, S. K. Choi, and C. H. Park, Diffuse dielectric anomaly in perovskite-type ferroelectric oxides in the temperature range of 400–700°C, J. Appl. Phys. **94**, 1904 (2003).

[99] M. Tyunina, J. Peräntie, T. Kocourek, S. Saukko, H. Jantunen, M. Jelinek, and A. Dejneka, Oxygen vacancy dipoles in strained epitaxial BaTiO$_3$ films, Phys. Rev. Res. **2**, 023056 (2020).

[100] P. Erhart, P. Träskelin, and K. Albe, Formation and switching of defect dipoles in acceptor-doped lead titanate: A kinetic model based on first-principles calculations, Phys. Rev. B **88**, 024107 (2013).

[101] O. Bidault, P. Goux, M. Kchikech, M. Belkaoumi, and M. Maglione, Space-charge relaxation in perovskites, Phys. Rev. B **49**, 7868 (1994).